Nano Res (2009) 2: 891–902
DOI 10.1007/s12274-009-9092-x
Research Article

Fine Tuning of the Sizes and Phases of ZrO_2 Nanocrystals

Xiangxing Xu and Xun Wang (✉)

Department of Chemistry, Tsinghua University, Beijing 100084, China

Received: 10 June 2009 / Revised: 23 August 2009 / Accepted: 8 October 2009

ABSTRACT

Monodisperse and pure phase zirconia (tetragonal: T-ZrO_2; monoclinic: M-ZrO_2) nanocrystals with finely tuned sizes as well as ultrathin T-ZrO_2 nanowires have been selectively synthesized by a facile solvothermal method. For the first time, a diagram of the size to effective strain was mapped for both T-ZrO_2 and M-ZrO_2, which gives a good explanation for the size- and cation doping-dependent stability of the two phases on the sub-10 nm scale. This work may expand our understanding of the phase properties of not only zirconia, but also various other polymorphic nanocrystals.

KEYWORDS

Nanocrystals, polymorphism, phase stability

Introduction

Nanocrystalline zirconia has attracted considerable attention recently for its technological importance as a ceramic component, and as a catalyst for various reactions. Pure zirconia exhibits polymorphism, being cubic at high temperature (> 2300 °C), tetragonal at intermediate temperature, and monoclinic at relatively low temperature (< 1100 °C). The tetragonal-monoclinic martensitic phase transformation of zirconia can also be triggered by stresses, accompanied by a volume change. Zirconia (or doped zirconia) dispersed in ceramics has long been applied to increase the fracture toughness, strength, and hardness [1–3]. A widely used catalyst and catalyst support, zirconia catalyzes alcohol dehydration [4, 5], CO/CO_2 hydrogenation [6], alkane isomerization [7], selective oxidation of alcohols and alkanes [8, 9], hydrogenation of olefins [10], and isomerization of olefins and epoxides [11, 12]. Different zirconia phases (monoclinic and tetragonal) exhibit different catalyst selectivities, such as in the selective hydrogenation of CO and alkane isomerization reactions [13–15]. Besides, ZrO_2 also finds applications as fuel cell electrode materials [16], chemical sensors [17, 18], heat resistant coatings [19], optical coatings [20], and high-*k* dielectric materials [21], etc.

Since it is recognized that well crystallized nanocrystals will lead to improved mechanical, chemical, and catalytic properties [22–24], various methods have been developed to synthesize zirconia nanocrystals, including hydrothermal synthesis [25], sol–gel synthesis [26], spray pyrolysis [27], mechanochemical processing [28], and two-phase synthesis [29]. Most of these products suffer from broad particle size distributions and severe aggregation, however. To enhance the performance, materials with well-defined phase,

Address correspondence to wangxun@mail.tsinghua.edu.cn

size, and morphology are required. Hyeon et al. reported a nonhydrolytic sol–gel reaction between zirconium(IV) n-propoxide and zirconium(IV) chloride at 340 °C to synthesize monodispersed tetragonal (T-ZrO_2) nanocrystals [30]. Zhao et al. developed a two-phase approach for the synthesis of shape-controlled zirconia nanocrystals from zirconium(IV) n-propoxide, but the product suffered from the presence of polymorphs: both monoclinic and tetragonal phases co-existed [31]. Therefore, the synthesis of monodisperse pure-phase T-ZrO_2 and monoclinic (M-ZrO_2) nanocrystals with good size controllability is urgently required. In this paper, we report a new single-phase solution method to synthesize monodisperse pure T-ZrO_2 and M-ZrO_2 nanocrystals with finely tuned sizes, as well as T-ZrO_2 ultrathin nanowires. The stabilization of T-ZrO_2 with yttrium(III) doping was also investigated. The resulting materials show unique phase related size–strain features.

1. Experimental

1.1 Preparation of zirconyl oleate

1.6 g of $ZrOCl_2 \cdot 8H_2O$ (AR, Sinopharm Chemical Reagent Co.) was dissolved in 10 mL of deionized H_2O to form solution A; 3.1 g of sodium oleate (> 98%, Beijing Chemical Reagent Co.) was ultrasonically dissolved in 20 mL of deionized H_2O and 25 mL of ethanol (AR) to form solution B. Then solutions A and B were mixed. Excess cyclohexane (40 mL) was added in order to extract zirconyl oleate, with stirring for 20 min. The upper organic layer was separated, the cyclohexane was distilled off, and the residue washed with water and dried to give zirconyl oleate. Yttrium oleate was prepared in a similar way by using $Y(NO_3)_3 \cdot 6H_2O$.

1.2 A typical synthesis of M-ZrO_2 nanocrystals

0.5 g of zirconyl oleate was dissolved in a mixture of 8 mL of oleic acid (AR), 1 mL of oleylamine (C_{18}-content 80%–90%, Acros), and 4 mL of ethanol. The mixture was transferred into a Teflon-lined stainless steel autoclave and heated at 200 °C for 2 days. After cooling down, excess ethanol was added to precipitate the white product, which was collected by centrifugation, further washed twice by cyclohexane and ethanol and redispersed in a nonpolar solvent such as cyclohexane to form a clear solution. The sizes of the M-ZrO_2 nanocrystals can be tuned from 8.0 nm to 2.8 nm by shortening the reaction time from 2 days to 4 h. When n-butanol was used in place of ethanol, flower- or string-like M-ZrO_2 nanocrystals structures were obtained. The influence of the chain length of the alcohol on the phase of ZrO_2 obtained is discussed below.

1.3 Synthesis of T-ZrO_2 nanocrystals

0.5 g of zirconyl oleate was dissolved in a mixture of 0.4 mL of oleic acid, 1 mL of oleylamine, and 10 mL of n-octane (AR). The mixture was allowed to react at 200 °C for 2 days. The sizes of the T-ZrO_2 nanocrystals can be tuned from 3.0 nm to 0.8 nm by shortening the reaction time from 2 days to 4 h. Using n-hexanol in place of ethanol also yielded T-ZrO_2 nanocrystals.

1.4 Synthesis of T-ZrO_2 ultrathin nanowires

0.5 g of zirconyl oleate was dissolved in a mixture of 1 mL of oleylamine and 10 mL of cyclohexane. The mixture was reacted at 200 °C for 3 days. The white gel-like product was ultrasonically washed with cyclohexane.

1.5 Synthesis of yttrium doped T-ZrO_2 nanocrystals

An appropriate amount of yttrium oleate was added to the system used to synthesize M-ZrO_2 nanocrystals.

1.6 Characterization

The phase purity of the products was verified by powder X-ray diffraction (XRD) on a Bruker D8 Advance X-ray diffractometer using Cu K_α radiation (λ = 1.5418 Å). The sizes and morphologies of the nanocrystals were measured using a JEOL JEM-1200EX transmission electron microscope (TEM) at 120 kV, and a Tecnai G2 F20 S-Twin high-resolution transmission electron microscope (HRTEM) at 200 kV. UV-vis absorption spectra were measured on a Hitachi U-3010 spectrophotometer. Photoluminescence (PL) spectra were recorded with a Hitachi F-4500 fluorescence spectrophotometer. FT-

IR spectroscopy was performed using a Nicolet 560 spectrometer.

2. Results and discussion

2.1 Phase and structure characterization

TEM and HRTEM images of the M-ZrO_2 nanocrystals, T-ZrO_2 nanocrystals, and T-ZrO_2 ultrathin nanowires are shown in Fig. 1. The XRD patterns indicate that both the M-ZrO_2 and T-ZrO_2 nanocrystals/nanowires are phase pure, agreeing well with JCPDS # 88-2390 and JCPDS # 80-0965, respectively. The T-ZrO_2 ultrathin nanowires are curved and branched in morphology and have broadened XRD peaks, indicating an ultra-small diameter. Measured from the HRTEM images (see Figs. 1(g) and 1(h)), the average diameter of the T-ZrO_2 nanowires is ~1.2 nm, consistent with the XRD result. The M-ZrO_2 nanocrystals are irregular in shape, while the T-ZrO_2 nanocrystals have a relatively spherical shape. The sizes of the M-ZrO_2 and T-ZrO_2 nanocrystals can be tuned from 8.0 nm to 2.8 nm, and 3.0 nm to 0.8 nm, respectively, by shortening the reaction time from 2 days to 4 h. Based on the formalism of Filipovich and Kalinina [32], Garvie, Mitsuhashi, Bailey, et al. predicted that T-ZrO_2 (as spherical crystals) should be the stable phase (not metastable) below a critical size of about 10 nm at 298 K [33–38]. However, our results show that, both pure T-ZrO_2 and M-ZrO_2

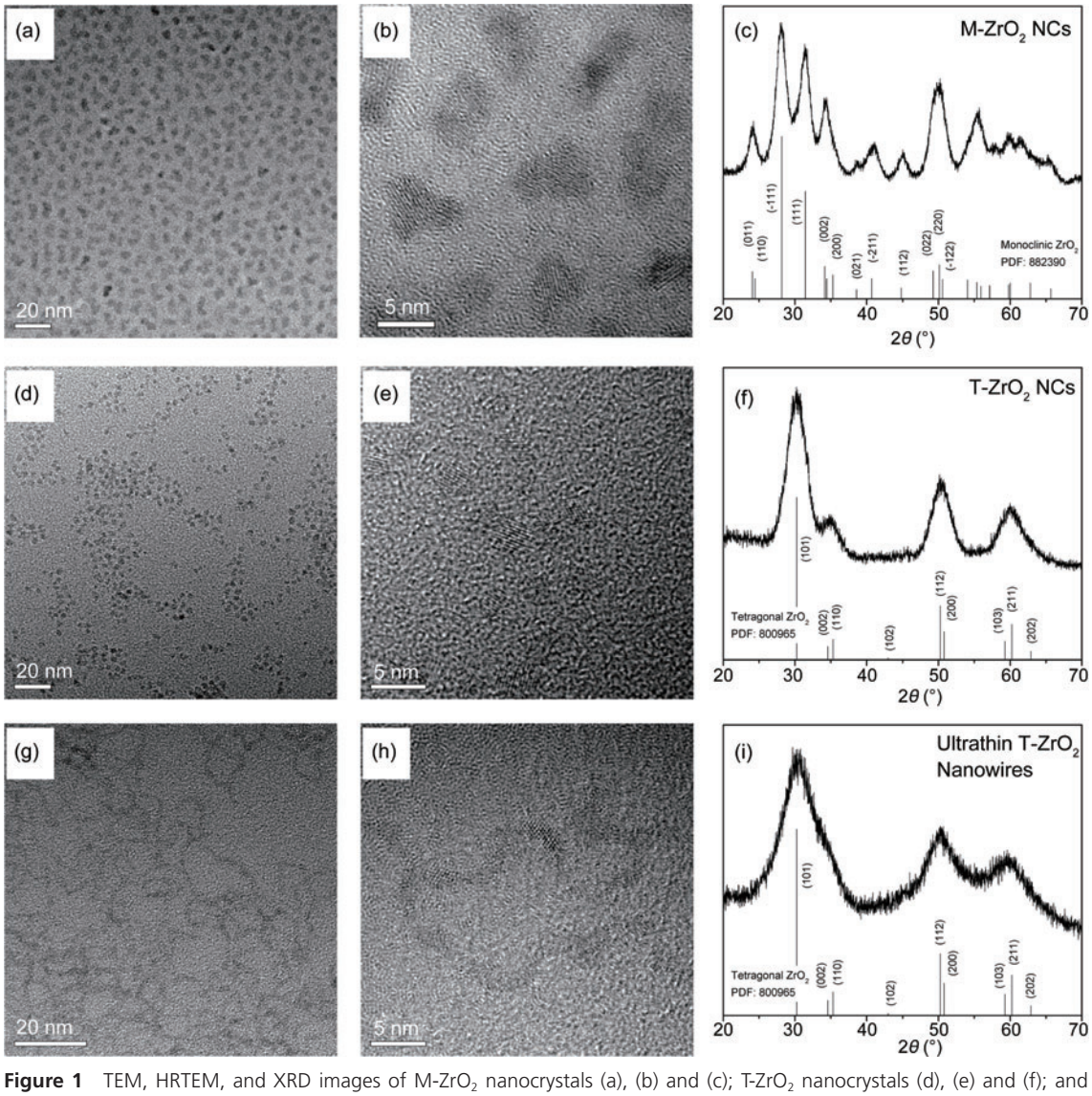

Figure 1 TEM, HRTEM, and XRD images of M-ZrO_2 nanocrystals (a), (b) and (c); T-ZrO_2 nanocrystals (d), (e) and (f); and ultrathin T-ZrO_2 nanowires (g), (h) and (i), respectively

nanocrystals within this size limit can be stabilized at ambient temperature, indicating that special stabilizing mechanisms are in operation. The fine controllability of the nanocrystal sizes of pure phase T-ZrO_2 and M-ZrO_2 in the range < 10 nm gives an ideal opportunity to probe deeper into the physics of the nano size-related phase transformation/stability.

2.2 Control of morphology: Effect of acid and amine

In the synthesis of ultrathin T-ZrO_2 nanowires, only oleylamine (without oleic acid) was utilized as the capping agent. By controlling the reaction time, it was found that the formation of the nanowires followed a typical oriented attachment growth mechanism. In the primary stage, T-ZrO_2 nanocrystal seeds were incubated. Then the seeds aggregated and attached. Finally, the ripened nanowires came into being. When a smaller amount of oleic acid (0.1 mL) was used in place of that (0.4 mL) required to synthesize T-ZrO_2 nanocrystals in n-octane with the same amount of oleylamine (1 mL), a pearl-string like structured T-ZrO_2 appeared (Figs. 2(d) and 2(e)), which we believe is an intermediate stage in the synthesis of the ripened nanowires. It probably arises because the oleylamine was selectively anchored to some specific T-ZrO_2 surfaces (or capping less tightly to some faces), facilitating the oriented attachment along the less capped crystal planes; the oleic acid was less sensitive to different nanocrystal planes and capped all the surfaces indiscriminately (or capping more tightly), therefore, prohibiting the attachment of other seeds and resulting in the formation of dispersed nanocrystals instead of the ultrathin nanowires. This is consistent with the Derjaguin–Landau–Verwey–Overbeek (DLVO) model, which states that higher surface covering ratios of ligands lead to larger steric repulsion between nanocrystals, and therefore the oriented attachment is weakened [39–43]. The increase in size (compare Figs. 1(g), 1(h) and Figs. 2(d), 2(e)) confirms this hypothesis: under conditions of less capping, the nucleation is boosted; in contrast, under conditions of strong capping and/or longer chain solvents, the nucleation is retarded and growth dominates. The schematic mechanism is shown in Fig. 2(f). The selective capping property of oleylamine has also been suggested as a reason for the formation of other ultrathin nanowires, e.g., SnO_2, InOOH, and Au [44–46]. The FT-IR measurements also provide supporting evidence (Figs. 2(g) and 2(h)). The C=O stretching vibration mode at 1738 cm^{-1} was clearly observed in the FT-IR spectrum of T-ZrO_2 nanocrystals, which were synthesized in the oleic acid-containing system. The peak shifts from that of free oleic acid at 1708 cm^{-1}, indicating the coordination interaction with the nanocrystals. The bands in the range 2800–3000 cm^{-1} are the CH_2 and CH_3 symmetric and asymmetric stretching vibrations. The broad peak at ~3400 cm^{-1} is assigned to absorbed H_2O or O–H groups. The multiple peaks in the range 1000–1700 cm^{-1} can be assigned to the N–H, C–H, COO^-, and H_2O modes or their mixtures. The strong peaks in the range 400–700 cm^{-1} are Zr–O vibration modes.

2.3 Phase control: Effect of alcohols with different chain length

By introducing ethanol into the system, we found that pure monoclinic phase zirconia nanocrystals were obtained. Zhao and co-workers have previously reported that, when increasing the hydrocarbon chain length of the capping agents (carboxylic acids), the fraction of monoclinic zirconia decreased [31]. In our synthesis system, a similar effect was found in that, when substituting ethanol with a longer chain alcohol (n-hexanol), pure tetragonal phased zirconia nanocrystals were obtained. This suggests that the formation of either a tetragonal or a monoclinic phase was determined by different reaction kinetic process. The pyrolysis of zirconyl oleate yields T-ZrO_2, while the alcohol-induced esterification and hydrolysis reactions prevail [44, 47], M-ZrO_2 is obtained. When shortening the reaction time, only an amorphous precursor (neither T-ZrO_2 nor M-ZrO_2) could be separated before M-ZrO_2 nucleation. The results differ from the size-related T-ZrO_2–M-ZrO_2 martensitic transformation that was indicated in the two-phase synthesis system, in which the M-ZrO_2 volume fraction increased with increasing size during the reaction stages [31]. This suggests an alternative mechanism in which the reaction-growth type (pyrolysis vs. esterification/hydrolysis) could be responsible for the T-ZrO_2 or M-ZrO_2 nucleation;

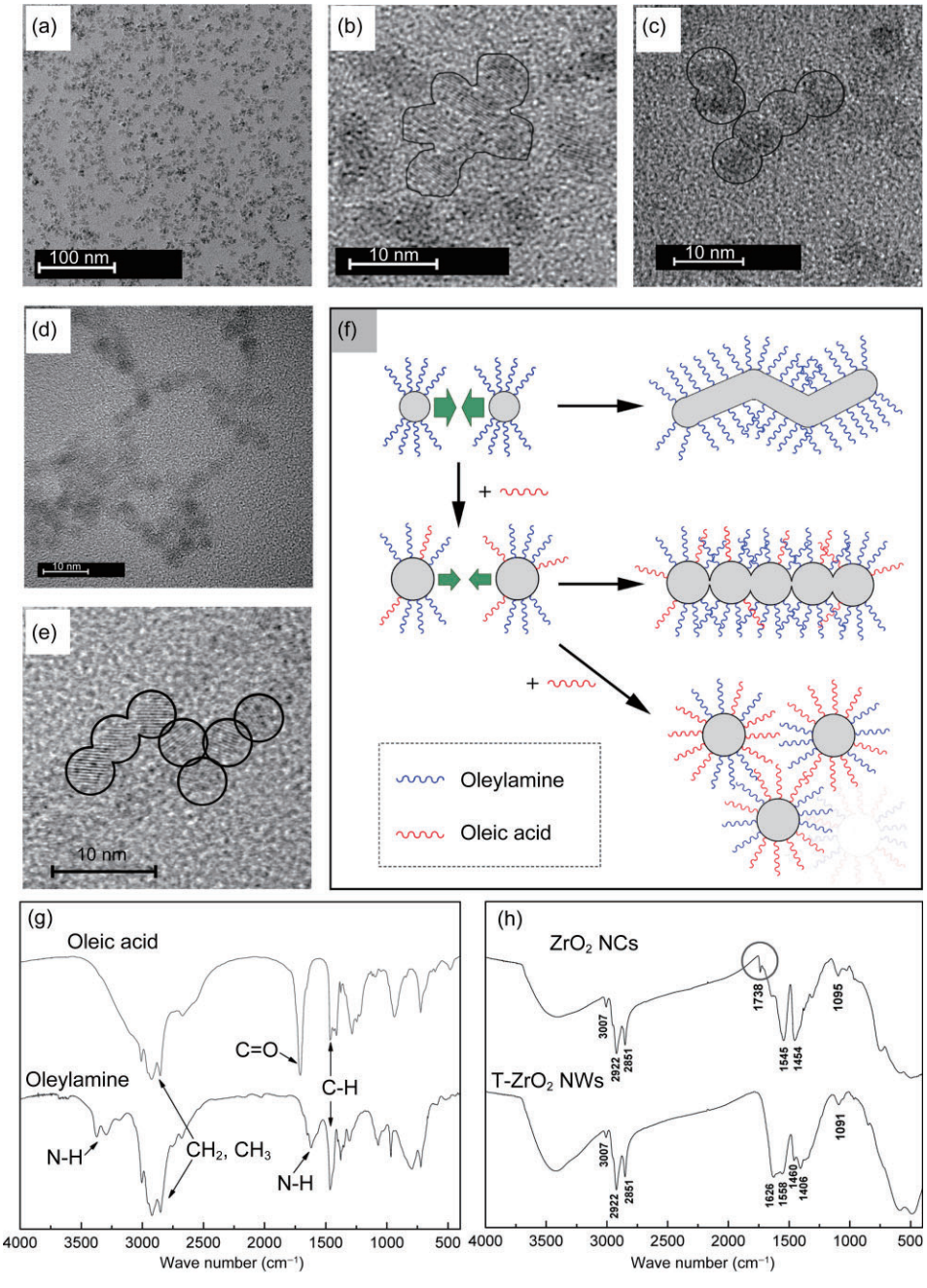

Figure 2 (a)–(c) Attached M-ZrO_2 nanocrystals showing flower- or string-like structures. (d), (e) Pearl-string like structured T-ZrO_2 was obtained when a smaller ratio of oleic acid to oleylamine was present than that required for synthesis of T-ZrO_2 NWs. (f) Schematic illustration of the different capping properties of oleylamine and oleic acid that result in the formation of zirconia nanowires and separate nanocrystals depending on the ratio of the capping species, and the evidence for this mechanism found in the FT-IR spectra (g) and (h)

this is further supported by the size–strain analysis discussed below. Otherwise, the T-ZrO_2 nucleation and martensitic transformation will be triggered instantaneously and essentially simultaneously such that they can hardly be separated. When n-butanol, an alcohol with medium chain length, was used, the as synthesized M-ZrO_2 nanocrystals tended to attach to form flower- or string-like structures, as shown in Figs. 2(a)–2(c). This can be understood in terms of the effective dielectric constant tuned attachment mechanism [44].

2.4 Doping-induced phase stabilization

It has long been recognized that the polymorphism of zirconia can be tuned by cation doping (Y^{3+}, Yb^{3+}, Ca^{2+}, Mg^{2+}, Ce^{4+}, etc.) [48, 49]. Of these, yttrium(III) is widely used as a stabilizer of the tetragonal phase. When yttrium oleate was introduced into the typical M-ZrO_2 synthesis system, yttrium-stabilized T-ZrO_2 nanocrystals were obtained. The TEM image is shown in Fig. 3(a) and the X-ray energy dispersive spectra (EDS) in Fig. 3(b) confirm that the yttrium content increases with the doping level. A similar stabilization was achieved when using lanthanide ions (e.g., Eu^{3+}, Yb^{3+}). The XRD peaks undergo a gradual broadening and a shift to the small angle direction when the Y^{3+} doping level increases from 2% to 30% (cation ratio, ±1.2% from the EDS quantitative analysis), indicating a decrease of crystallite size and increase of lattice constant, respectively (Figs. 3(c)–3(e)). This is consistent with the fact that the radius of Y^{3+} (0.102 nm) is larger than that of Zr^{4+} (0.084 nm). The monoclinic phase was retained when yttrium oleate is added in the ripening stage of M-ZrO_2. Therefore, the ion doping must occur during the ZrO_2 nucleation and growth stages.

2.5 Dissolution–recrystallization phase transformation

The T-ZrO_2 to M-ZrO_2 transformation was also revealed by hydrothermally treating T-ZrO_2 nanocrystals at 200 °C under basic conditions (NaOH: 1–5 mol/L). The as formed M-ZrO_2 nanocrystals have a size of 20–100 nm. The dissolution–recrystallization mechanism is believed to be responsible for the phase transformation.

2.6 Strain in zirconia nanocrystals

The existence of different nanocrystal phases at room temperature depends on two aspects. One is the historical kinetic factor in the nucleation-

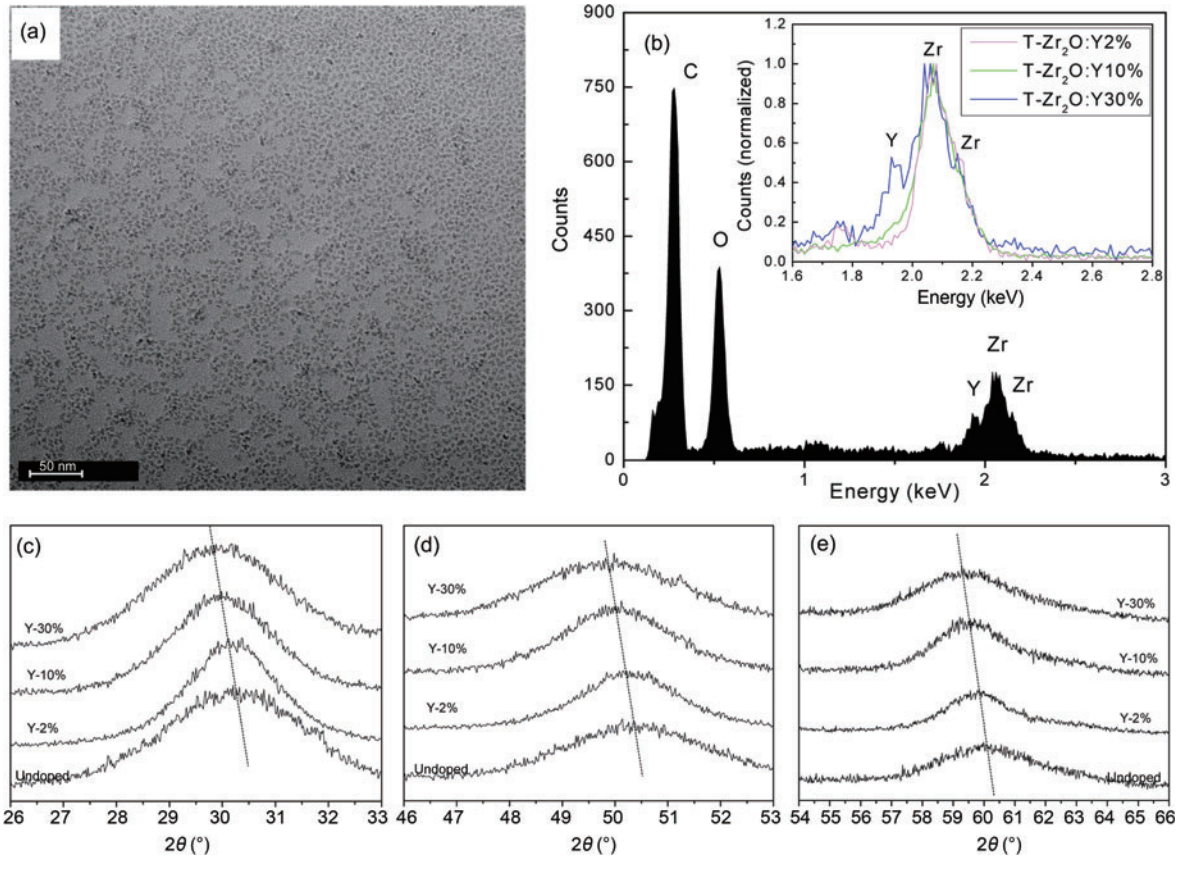

Figure 3 (a) TEM image of the yttrium doped T-ZrO_2 nanocrystals. (b) EDS spectrum showing a 30% Y-doping, with the insert showing Y-doping of 2%, 10%, and 30%. (c)–(e) XRD patterns showing the shift of diffraction peaks to small angle with the increasing doping fraction of yttrium

growth stages; the other is the thermodynamic principle. The former is often associated with non-equilibrium growth processes, while the later is mainly governed by the total energies of the surface and bulk, and the strain. Holmes et al. measured the heat of immersion of T-ZrO_2 and M-ZrO_2 prepared by calcining zirconium hydroxide in the range 600–1000 °C. They concluded that M-ZrO_2 has a higher surface energy [34]. The heat of the T-ZrO_2–M-ZrO_2 transformation/unit volume and transformation temperature is also known. Garvie et al. indicated that T-ZrO_2 should be a more stable phase than M-ZrO_2 below a critical particle size of 10 nm at temperatures much lower than the bulk transformation temperature [37]. However, our results showed that not only pure T-ZrO_2, but also pure M-ZrO_2 nanocrystals, can be synthesized within this size limit and stabilized at room temperature. Therefore, the third factor—the intrinsic strain—should be taken into account.

The Williamson–Hall equation was applied to deduce the effective strain from the XRD data [50–52]:

$$\frac{\beta\cos\theta}{\lambda} = \frac{1}{\delta} + \frac{2\eta\sin\theta}{\lambda} \quad (1)$$

where θ is the Bragg angle of the peak, λ is the X-ray wavelength, δ is the effective particle size, η is the effective strain, and β is the full width at half maximum (FWHM, in radians) estimated by the following equation:

$$\beta = \frac{\beta_{1/2} - \beta_p}{0.89} \quad (2)$$

where $\beta_{1/2}$ and β_p are the FWHMs obtained for nanocrystals and micron-sized powders, respectively. Here $\beta_p = 0.25°$ is taken as a constant. $\beta_{1/2}$ is extracted from the XRD patterns by Lorentzian multi-peak fitting. To extract the effective strain (η) from the XRD patterns, (101), (112), and (211) peaks were selected for T-ZrO_2, and (-111), (111), and (220) were selected for M-ZrO_2. An approximation was made that very adjacent XRD peaks have the same FWHM value. For T-ZrO_2, we assumed $FWHM_{(112)} = FWHM_{(200)}$, $FWHM_{(211)} = FWHM_{(103)}$; and for M-$ZrO_2$, we assumed $FWHM_{(-212)} = FWHM_{(022)} = FWHM_{(200)} = FWHM_{(-122)} = FWHM_{(-221)}$. No shape factor of the nanocrystals was included. The Scherrer equation was applied to calculate the nanocrystal size, using the Lorentzian multi-peak fitting data $\beta_{1/2}$ and θ. For T-ZrO_2, the size is the average value of (101), (112), and (211); for M-ZrO_2, the size is the average value of (111) and (-111).

A negative slope (η) of the linear fit of $\beta\cos\theta$ to $2\sin\theta$ is indicative of compressive strain. The calculated nanocrystal size and the effective strain (η) are mapped in Fig. 4(c) (The calculation data can be found in Table S-1). For M-ZrO_2, the compressive strain increases with decreasing nanocrystal size; in contrast, for T-ZrO_2, the effective strain fluctuates around zero, indicating a relaxed strain state. For nanocrystals of the same size < 10 nm, M-ZrO_2 endures larger compressive strain than T-ZrO_2. The size-related difference $\Delta\eta$ contributes to the total energy of the material. Therefore, for the first time, this gives direct evidence that T-ZrO_2 can be more stable than M-ZrO_2 for limited crystallite sizes, as a result of strain–size concerns. This is consistent with the theoretically calculated critical value of 10 nm, and also with the value of 30 nm calculated in the case of polymorphs with interfacial energies counted. Since the compressive strain increased drastically when the nanocrystal size was < 5 nm for M-ZrO_2, this gives a convincing explanation for the fact that M-ZrO_2 nanocrystals with size < 2.8 nm cannot be synthesized. From another perspective, a high intrinsic compressive strain is indispensable for the stabilization of M-ZrO_2 nanocrystals with size < 10 nm. This is a likely reason why the martensitic transformation was not observed in our experiments.

The size-related effective strains can also be affected by doping. When the doping level was increased from 2% to 30%, the size of the Y:T-ZrO_2 nanocrystals decreased. The effective strain of 2%Y:T-ZrO_2 falls between the T-ZrO_2 and M-ZrO_2 gap, while 10% and 30%Y:T-ZrO_2 fit well within the pure T-ZrO_2 region. This indicates that doping with yttrium ions alleviates the compressive strain, and thus, yields the tetragonal phase.

2.7 Photoluminescence (PL) properties

The UV-vis absorption spectra of T-ZrO_2 and M-ZrO_2 nanocrystals are shown in Figs. 5(a) and 5(b). Since

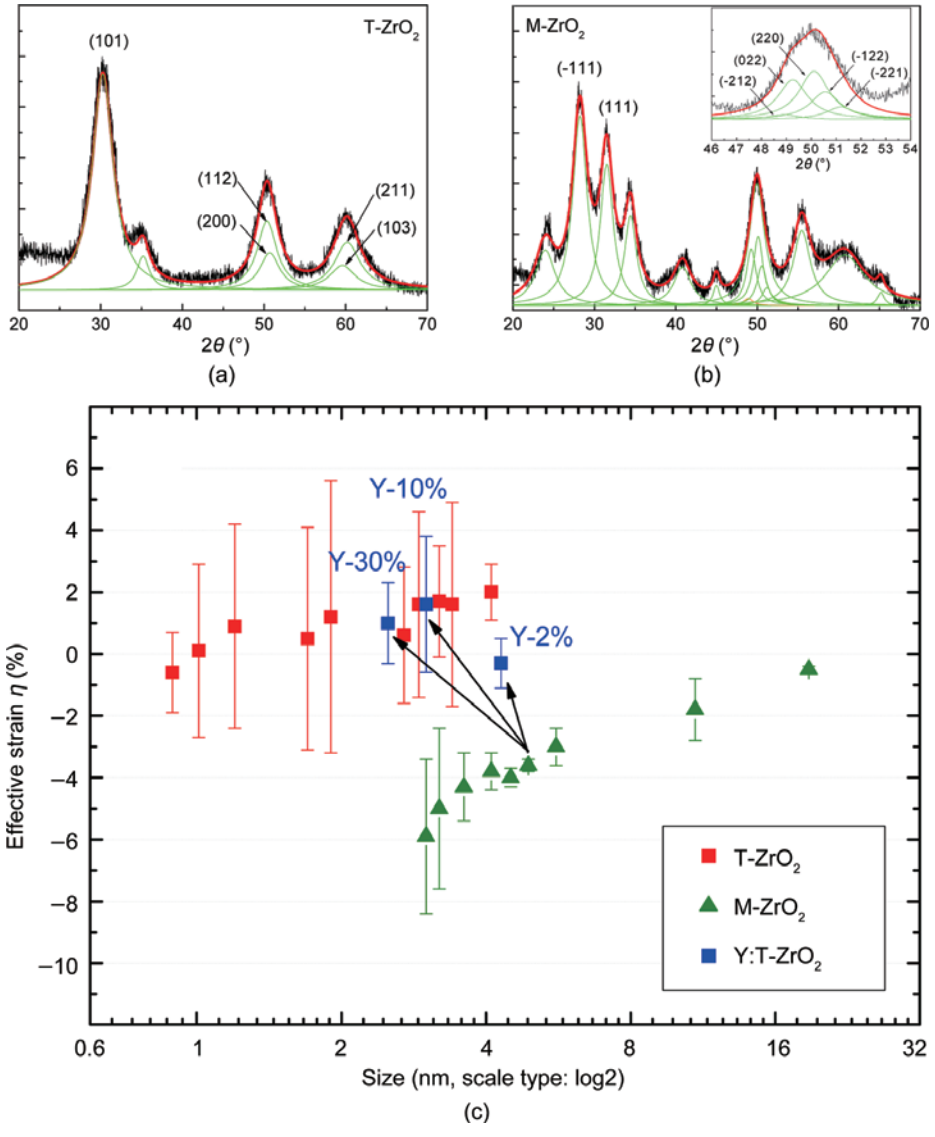

Figure 4 (a) A typical T-ZrO_2 XRD pattern with Lorentzian multi-peak fitting. (b) A typical M-ZrO_2 XRD pattern with Lorentzian multi-peak fitting. (c) Effective strain to nanocrystal size diagram for T-ZrO_2, M-ZrO_2 and Y:T-ZrO_2. The starting end of the arrows indicate the M-ZrO_2 synthesis system that was adapted to synthesize Y:T-ZrO_2 nanocrystals

bulk ZrO_2 of either monoclinic or tetragonal phase has a forbidden band of about 4.9–5.0 eV [53, 54], the observed peak within the range 4.8–5.2 eV can be identified as the band gap absorption.

Figures 5(c) and 5(d) show the PL spectra measured for ZrO_2 dispersed in cyclohexane. The spectra range from ultraviolet (300 nm) to the visible (600 nm). Although still somewhat controversial, it is generally accepted that for various oxide/sulfide nanomaterials, such as ZnS, ZnO, SnO_2, SiO_2, In_2O_3, and ZrO_2, the relatively broad PL spectra arise from emission of the oxygen or sulfur defect states [30, 44, 45, 55–58]. The PL intensity of the yttrium-doped ZrO_2 nanocrystals was stronger than undoped samples, indicating higher defect density. For T-ZrO_2, the PL spectrum peak shifted from 337 nm to 396 nm when the size increased from ~1 nm to ~3 nm. The PL spectrum of 2%Y:T-ZrO_2 with a size ~5 nm showed a further red-shift to 458 nm. For M-ZrO_2, the PL spectrum peak shifted from 402 nm to 442 nm when the size increased from ~4 nm to ~5 nm. Similar size-related PL properties have also been reported for the wide band semiconductors SnO_2 and ZnS as nanocrystals and as nanorods/ultrathin nanowires

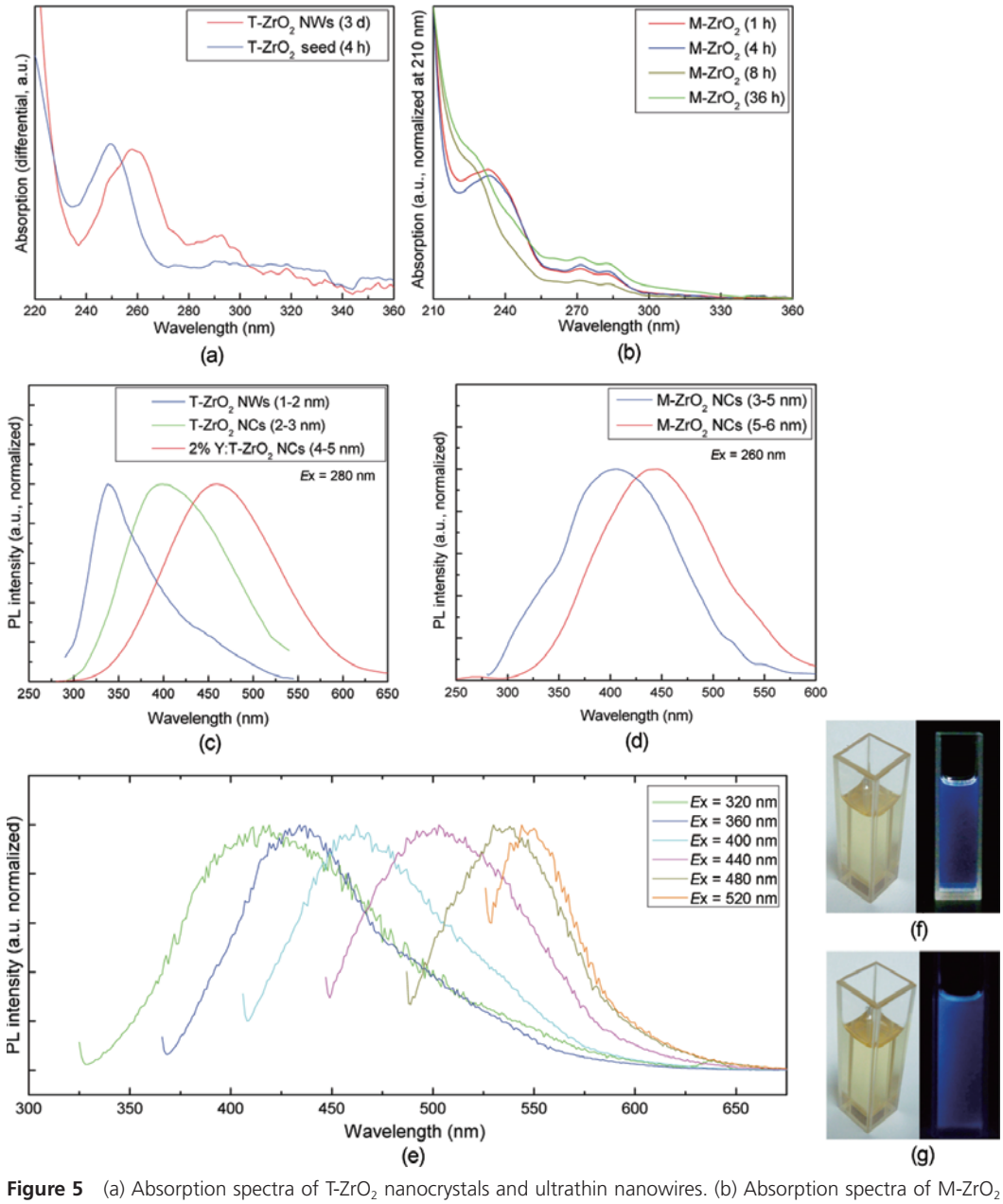

Figure 5 (a) Absorption spectra of T-ZrO_2 nanocrystals and ultrathin nanowires. (b) Absorption spectra of M-ZrO_2 nanocrystals. (c) PL spectra of T-ZrO_2. (d) PL spectra of M-ZrO_2 nanocrystals. (e) PL spectra of M-ZrO_2 nanocrystals (5–6 nm) with different excitation wavelengths. (f) and (g) Images of T-ZrO_2 and M-ZrO_2 nanocrystals, respectively, dispersed in cyclohexane and their fluorescence under 365 nm excitation

[44, 57]. Figure 5(e) shows that by changing the excitation wavelength from 320 nm to 520 nm, the PL spectrum peak shifted accordingly. It was noticed that when the excitation wavelength exceeded 400 nm, the PL intensity decreased drastically.

3. Conclusions

M-ZrO_2 nanocrystals, pure and yttrium-doped T-ZrO_2 nanocrystals, and ultrathin T-ZrO_2 nanowires have been successfully synthesized using a solvothermal method. The nanocrystal size, morphology, and phase can be well controlled by tuning the reaction system and by doping. The effective compressive strain in the M-ZrO_2 nanocrystals increases with decreasing nanocrystal size. The difference in the strain-size diagrams of M-ZrO_2 and T-ZrO_2 gives direct evidence for the stability of T-ZrO_2 and M-ZrO_2 nanocrystals at room temperature. The controllability of the zirconia phases, morphologies, and sizes provides

the basis for their surface and energy structure design. Therefore, tunable structural, semiconductor, and catalytic properties can be expected for such materials.

Acknowledgements

The authors thank the National Natural Science Foundation of China (Nos. 20725102 and 50772056), the Foundation for the Authors of National Excellent Doctoral Dissertation of China, the Program for New Century Excellent Talents of the Ministry of Education of China, the Fok Ying Tung Education Foundation (111012), and the State Key Project of Fundamental Research for Nanoscience and Nanotechnology (2006CB932301) for financial support.

Electronic Supplementary Material: Supplementary material is available in the online version of this article at http://dx.doi.org/10.1007/s12274-009-9092-x and is accessible free of charge. It contains the enlarged images of Figs. 1(b), 1(e), and 1(h), Figs. 2(b), 2(d), and 2(e), showing the microstructure details of the ZrO_2 nanocrystals, and details of the calculations using XRD data to obtain nanocrystal size, effective strain, and error bars.

References

[1] Garvie, R. C.; Hannink, R. H.; Pascoe, R. T. Ceramic steel. *Nature* **1975**, *258*, 703–704.

[2] Hirvonen, A.; Nowak, R.; Yamamoto, Y.; Sekino, T.; Niihara, K. Fabrication, structure, mechanical and thermal properties of zirconia-based ceramic nanocomposites. *J. Eur. Ceram. Soc.* **2006**, *26*, 1497–1505.

[3] Duszovda, A.; Dusza, J.; Tomasek, K.; Blugan, G.; Kuebler, J. Microstructure and properties of carbon nanotube/zirconia composite. *J. Eur. Ceram. Soc.* **2008**, *28*, 1023–1027.

[4] Larsen, G.; Lotero, E.; Petkovic, L. M.; Shobe, D. S. Alcohol dehydration reactions over tungstated zirconia catalysts. *J. Catal.* **1997**, *169*, 67–75.

[5] Wilson, N. G.; McCreedy, T. On-chip catalysis using a lithographically fabricated glass microreactor—The dehydration of alcohols using sulfated zirconia. *Chem. Commun.* **2000**, 733–734.

[6] Weigel, J.; Koeppel, R. A.; Baiker, A.; Wokaun, A. Surface species in CO and CO_2 hydrogenation over copper/zirconia: On the methanol synthesis mechanism. *Langmuir* **1996**, *12*, 5319–5329.

[7] Kuba, S.; Gates, B. C.; Grasselli, R. K.; Knozinger, H. An active and selective alkane isomerization catalyst: Iron- and platinum-promoted tungstated zirconia. *Chem. Commun.* **2001**, 321–322.

[8] Wang, S. B.; Murata, K.; Hayakawa, T.; Hamakawa, S.; Suzuki, K. Selective oxidation of ethane and propane over sulfated zirconia-supported nickel oxide catalysts. *J. Chem. Technol. Biotechnol.* **2001**, *76*, 265–272.

[9] Li, W. Z.; Huang, H.; Li, H. J.; Zhang, W.; Liu, H. C. Facile synthesis of pure monoclinic and tetragonal zirconia nanoparticles and their phase effects on the behavior of supported molybdena catalysts for methanol-selective oxidation. *Langmuir* **2008**, *24*, 8358–8366.

[10] Yamaguchi, T.; Hightower, J. W. Hydrogenation of 1,3-butadiene with 1,3-cyclohexadiene and molecular deuterium over zirconium dioxide catalysts. *J. Am. Chem. Soc.* **1977**, *99*, 4201–4203.

[11] Arata, K.; Akutagawa, S.; Tanabe, K. Epoxide rearrangement III. Isomerization of 1-methylcyclohexene oxide over TiO_2–ZrO_2, $NiSO_4$ and $FeSO_4$. *Bull. Chem. Soc. Jpn.* **1976**, *49*, 390–393.

[12] Nakano, Y.; Iizuka, T.; Hattori, H.; Tanabe, K. Surface properties of zirconium oxide and its catalytic activity for isomerization of 1-butene. *J. Catal.* **1979**, *57*, 1–10.

[13] Stichert, W.; Schuth, F.; Kuba, S.; Knozinger, H. Monoclinic and tetragonal high surface area sulfated zirconias in butane isomerization: CO adsorption and catalytic results. *J. Catal.* **2001**, *198*, 277–285.

[14] He, D. P.; Ding, Y. I.; Luo, H. Y.; Li, C. Effects of zirconia phase on the synthesis of higher alcohols over zirconia and modified zirconia. *J. Mol. Catal. A* **2004**, *208*, 267–271.

[15] Rhodes, M. D.; Bell, A. T. The effects of zirconia morphology on methanol synthesis from CO and H_2 over Cu/ZrO_2 catalysts: Part I. Steady-state studies. *J. Catal.* **2005**, *233*, 198–209.

[16] Mamak, M.; Coombs, N.; Ozin, G. A. Electroactive mesoporous yttria stabilized zirconia containing platinum or nickel oxide nanoclusters: A new class of solid oxide fuel cell electrode materials. *Adv. Funct. Mater.* **2001**, *11*, 59–63.

[17] Can, Z. Y.; Narita, H.; Mizusaki, J.; Tagawa, H. Detection of carbon monoxide by using zirconia oxygen sensor. *Solid State Ionics* **1995**, *79*, 344–348.

[18] Liu, G. D.; Lin, Y. H. Electrochemical sensor for organophosphate pesticides and nerve agents using zirconia nanoparticles as selective sorbents. *Anal. Chem.* **2005**, 77, 5894–5901.

[19] Izumi, K.; Murakami, M.; Deguchi, T.; Morita, A.; Tohge, N.; Minami, T. Zirconia coating on stainless steel sheets from organozirconium compounds. *J. Am. Ceram. Soc.* **1989**, *72*, 1465–1468.

[20] Taylor, D. P.; Simpson, W. C.; Knutsen, K.; Henderson, M. A.; Orlando, T. M. Photon stimulated desorption of cations from yttria-stabilized cubic ZrO_2 (100). *Appl. Surf. Sci.* **1998**, *127*, 101–104.

[21] Dutta, G.; Hembram, K. P. S. S.; Rao, G. M.; Waghmare, U. V. Effects of O vacancies and C doping on dielectric properties of ZrO_2: A first-principles study. *Appl. Phys. Lett.* **2006**, *89*, 202904.

[22] Wang, D. S.; Xie, T.; Li, Y. D. Nanocrystals: Solution-based synthesis and applications as nanocatalysts. *Nano Res.* **2009**, *2*, 30–46.

[23] Zhu, K. K.; Wang, D. H.; Liu, J. Self-assembled materials for catalysis. *Nano Res.* **2009**, *2*, 1–29.

[24] Peng, X. G. An essay on synthetic chemistry of colloidal nanocrystals. *Nano Res.* **2009**, *2*, 425–447.

[25] Piticescu, R. R.; Monty, C.; Taloi, D.; Motoc, A.; Axinte, S. Hydrothermal synthesis of zirconia nanomaterials. *J. Eur. Ceram. Soc.* **2001**, *21*, 2057–2060.

[26] Bokhimi, X.; Morales, A.; Novaro, O.; Portilla, M.; Lopez, T.; Tzompantzi, F.; Gomez, R. Tetragonal nanophase stabilization in nondoped sol–gel zirconia prepared with different hydrolysis catalysts. *J. Solid State Chem.* **1998**, *135*, 28–35.

[27] Mueller, R.; Jossen, R.; Pratsinis, S. E.; Watson, M.; Akhtar, M. K. Zirconia nanoparticles made in spray flames at high production rates. *J. Am. Ceram. Soc.* **2004**, *87*, 197–202.

[28] Zyryanov, V. V.; Uvarov, N. F.; Sadykov, V. A. Mechanochemical synthesis of solid solutions based on ZrO_2 and their electrical conductivity. *Glass Phys. Chem.* **2007**, *33*, 394–401.

[29] Tang, K. J.; Zhang, J. N.; Yan, W. F.; Li, Z. H.; Wang, Y. D.; Yang, W. M.; Xie, Z. K.; Sun, T. L.; Fuchs, H. One-step controllable synthesis for high-quality ultrafine metal oxide semiconductor nanocrystals *via* a separated two-phase hydrolysis reaction. *J. Am. Chem. Soc.* **2008**, *130*, 2676–2680.

[30] Joo, J.; Yu, T.; Kim, Y. W.; Park, H. M.; Wu, F. X.; Zhang, J. Z.; Hyeon, T. Multigram scale synthesis and characterization of monodisperse tetragonal zirconia nanocrystals. *J. Am. Chem. Soc.* **2003**, *125*, 6553–6557.

[31] Zhao, N. N.; Pan, D. C.; Nie, W.; Ji, X. L. Two-phase synthesis of shape-controlled colloidal zirconia nanocrystals and their characterization. *J. Am. Chem. Soc.* **2006**, *128*, 10118–10124.

[32] Filipovich, V. N.; Kalinina, A. M. *The Structure of Glass*; Toropov, N. A, Porai–Koshits, E. A., Eds.; Consultants Bureau: New York, 1965; Vol. 5, pp 34–38.

[33] Garvie, R. C. The occurrence of metastable tetragonal zirconia as a crystallite size effect. *J. Phys. Chem.* **1965**, *69*, 1238–1243.

[34] Holmes, H. F.; Fuller, E. L.; Gammage R. B. Heats of immersion in the zirconium oxide-water system. *J. Phys. Chem.* **1972**, *76*, 1497–1502.

[35] Bailey, J. E.; Lewis, D.; Librant, Z. M.; Porter, L. J. Phase transformations in milled zirconia. *Trans. J. Brit. Ceram. Soc.* **1972**, *71*, 25–30.

[36] Mitsuhashi, T.; Ichihara, M.; Tatsuke, U. Characterization and stabilization of metastable tetragonal ZrO_2. *J. Am. Ceram. Soc.* **1974**, *57*, 97–101.

[37] Garvie, R. C. Stabilization of the tetragonal structure in zirconia microcrystals. *J. Phys. Chem.* **1978**, *82*, 218–224.

[38] Garvie, R. C.; Goss, M. F. Intrinsic size dependence of the phase transformation temperature in zirconia microcrystals. *J. Mater. Sci.* **1986**, *21*, 1253–1257.

[39] de Gennes, P. G. Polymers at an interface: A simplified view. *Adv. Colloid Interface Sci*. **1987**, *27*, 189–209.

[40] Korgel, B. A.; Fullam, S.; Connolly, S.; Fitzmaurice, D. Assembly and self-organization of silver nanocrystal superlattices: Ordered "soft spheres". *J. Phys. Chem. B* **1998**, *102*, 8379–8388.

[41] Sinyagin, A. Y.; Belov, A.; Tang, Z. Y.; Kotov, N. A. Monte Carlo computer simulation of chain formation from nanoparticles. *J. Phys. Chem. B* **2006**, *110,* 7500–7507.

[42] Zhang, S. S.; Leem, G.; Srisombat, L. O.; Lee, T. R. Rationally designed ligands that inhibit the aggregation of large gold nanoparticles in solution. *J. Am. Chem. Soc.* **2008**, *130*, 113–120.

[43] Shen, S. L.; Zhuang, J.; Xu, X. X.; Nisar, A.; Hu, S.; Wang, X. Size effects in oriented–attachment growth process:

The case of Cu nanoseeds. *Inorg. Chem.* **2009**, *48*, 5117–5128.

[44] Xu, X. X.; Zhuang, J.; Wang, X. SnO_2 quantum dots and quantum wires: Controllable synthesis, self-assembled 2D architectures, and gas-sensing properties. *J. Am. Chem. Soc.* **2008**, *130*, 12527–12535.

[45] Xu, X. X.; Wang, X. Size- and surface-determined transformations: From ultrathin InOOH nanowires to uniform c-In_2O_3 nanocubes and rh-In_2O_3 nanowires. *Inorg. Chem.* **2009**, *48*, 3890–3895.

[46] Huo, Z. Y.; Tsung, C. K.; Huang, W. Y.; Zhang, X. F.; Yang, P. D. Sub-two nanometer single crystal Au nanowires. *Nano Lett.* **2008**, *8*, 2041–2044.

[47] Narayanaswamy, A.; Xu, H. F.; Pradhan, N.; Kim, M.; Peng, X. G. Formation of nearly monodisperse In_2O_3 nanodots and oriented-attached nanoflowers: Hydrolysis and alcoholysis vs. pyrolysis. *J. Am. Chem. Soc.* **2006**, *128*, 10310–10319.

[48] Ingel, R. P.; Lewis, D. Lattice parameters and density for Y_2O_3-stabilized ZrO_2. *J. Am. Ceram. Soc.* **1986**, *69*, 325–332.

[49] Stefanovich, E. V.; Shluger, A. L.; Catlow, C. R. A. Theoretical study of the stabilization of cubic-phase ZrO_2 by impurities. *Phys. Rev. B: Condens. Matter* **1994**, *49*, 11560–11571.

[50] Hall, W. H. X-ray line broadening in metals. *Proc. Phys. Soc. London, Sect. A* **1949**, *62*, 741–743.

[51] Williamson, G. K.; Hall, W. H. X-ray line broadening from filed aluminium and wolfram. *Acta Metall.* **1953**, *1*, 22–31.

[52] Kang, J. Y.; Tsunekawa, S.; Kasuya. A. Ultraviolet absorption spectra of amphoteric SnO_2 nanocrystallites. *Appl. Surf. Sci.* **2001**, *174*, 306–309.

[53] Bendoraitis, J. G.; Salomon, R. E. Optical energy gap in the monoclinic oxides of hafnium and zirconium and their solid solutions. *J. Phys. Chem.* **1965**, *69*, 3660–3667.

[54] Emeline, A.; Kataeva, G. V.; Litke, A. S.; Rudakova, A. V.; Ryabchuk, V. K.; Serpone, N. Spectroscopic and photoluminescence studies of a wide band gap insulating material: Powdered and colloidal ZrO_2 sols. *Langmuir* **1998**, *14*, 5011–5022.

[55] Nishikawa, H.; Watanabe, E.; Ito, D.; Ohki, Y. Decay kinetics of the 4.4-eV photoluminescence associated with the two states of oxygen-deficient-type defect in amorphous SiO_2. *Phys. Rev. Lett.* **1994**, *72*, 2101–2104.

[56] Law, M.; Sirbuly, D. J.; Johnson, J. C.; Goldberger, J.; Saykally, R. J.; Yang, P. D. Nanoribbon waveguides for subwavelength photonics integration. *Science* **2004**, *305*, 1269–1273.

[57] Yu, J. H.; Joo, J.; Park, H. M.; Baik, S. I.; Kim, Y. W.; Kim, S. C.; Hyeon, T. Synthesis of quantum-sized cubic ZnS nanorods by the oriented attachment mechanism. *J. Am. Chem. Soc.* **2005**, *127*, 5662–5670.

[58] Tam, K. H.; Cheung, C. K.; Leung, Y. H.; Djurii, A. B.; Ling, C. C.; Beling, C. D.; Fung, S.; Kwok, W. M.; Chan, W. K.; Phillips, D. L.; Ding, L.; Ge, W. K. Defects in ZnO nanorods prepared by a hydrothermal method. *J. Phys. Chem. B* **2006**, *110*, 20865–20871.